International Journal of Hydrogen Energy 255 (2026) 156439

Contents lists available at ScienceDirect

International Journal of Hydrogen Energy

journal homepage: www.elsevier.com/locate/he

Electronic metal-support interaction in Ru–Co catalysts boosts H_2 generation via sodium borohydride hydrolysis

Chenxi Shang [a], Changtai Xu [a], Boxuan Lu [a], Shuyi Shang [a], Tayirjan Taylor Isimjan [b,*], Jingya Guo [a,**], Xiulin Yang [a,***]

[a] Guangxi Key Laboratory of Low Carbon Energy Materials, School of Chemistry and Pharmaceutical Sciences, Guangxi Normal University, Guilin, 541004, China
[b] Saudi Arabia Basic Industries Corporation (SABIC) at King Abdullah University of Science and Technology (KAUST), Thuwal, 23955-6900, Saudi Arabia

ARTICLE INFO

Keywords:
Core-shell nanostructure
Electronic metal–support interaction
Synergistic effect
Sodium borohydride
Hydrogen production

ABSTRACT

Developing high-efficiency and stable catalysts for $NaBH_4$ hydrolysis is critical for safe, high-density and on-demand hydrogen generation. Herein, a core-shell structured Co@SiO_2@C composite was fabricated as support to immobilize Ru nanoparticles, which precisely regulates electron-metal-support interactions (EMSI). The SiO_2 layer inhibits Ru aggregation and carbon layer accelerates electron transfer, synergistically optimizing Ru electron density and boosting Co–Ru dual active sites. The composite catalyst Co@SiO_2@C–Ru exhibits significantly enhanced catalytic performance, achieving a hydrogen production rate of 7783.2 mL min^{-1} g^{-1} at 25 °C, substantially surpassing most previously reported catalysts. Furthermore, the catalyst retains excellent catalytic activity after five cycles, demonstrating favorable structural and performance stability. Mechanism studies confirm that EMSI drives electron transfer from Co to Ru, optimizing BH_4^- adsorption and activation via Michaelis–Menten kinetics. This work offers a facile strategy for constructing high-performance dual-metal core-shell hydrolysis catalysts.

1. Introduction

The ongoing depletion of fossil fuel resources and the growing severity of global environmental issues have urgently driven the pursuit of sustainable and clean energy technologies to enable low-carbon energy transition [1]. Hydrogen, with its significantly higher energy density (120 MJ · kg^{-1}) compared to gasoline (44 MJ · kg^{-1}), and its production of only water as a by-product when used, is considered one of the most promising and environmentally friendly alternatives to traditional fossil fuels [2–4]. Common hydrogen storage candidates, including formic acid, methanol, ammonia and ethanol, are limited by flammability, corrosiveness and potential environmental risks [5]. In contrast, sodium borohydride ($NaBH_4$) stands out as a promising hydrogen supplier for organic synthesis and on-site hydrogen generation, benefiting from its high hydrogen capacity, non-toxicity, reliable operation, tunable dehydrogenation behavior and convenient storage and transportation [6–8]. Although the U.S. Department of Energy (DOE) previously issued a non-recommendation regarding the use of $NaBH_4$ hydrolysis in vehicle-mounted systems—primarily due to the high costs associated with its production and regeneration—the development of low-cost synthesis and regeneration technologies by a Japanese enterprise in 2019 has renewed interest in its potential for large-scale applications [9,10]. Despite the above progress, $NaBH_4$ itself has obvious drawbacks: its hydrolysis proceeds very slowly under ambient conditions, and the catalyst-free dehydrogenation process requires a high temperature of around 565 °C [11,12], making the design of high-performance catalysts essential to unlock its practical value.

In current research, ruthenium-based catalysts exhibit exceptional catalytic activity in the hydrolysis of $NaBH_4$ due to their unique electronic structure and moderate water-dissociation energy [13]. However, the scarcity and high cost of ruthenium severely limit its practical deployment [14]. To address this issue, researchers have explored combining ruthenium with other metals, with cobalt in particular shown to significantly enhance ruthenium's performance in $NaBH_4$ hydrolysis through multiple synergistic effects [1,15,16]. Nevertheless, monometallic Co nanoparticles suffer from severe agglomeration under

* Corresponding author.
** Corresponding author.
*** Corresponding author.
E-mail addresses: isimjant@sabic.com (T.T. Isimjan), jyguo@gxnu.edu.cn (J. Guo), xlyang@gxnu.edu.cn (X. Yang).

https://doi.org/10.1016/j.ijhydene.2026.156439
Received 16 May 2026; Received in revised form 20 June 2026; Accepted 3 July 2026
Available online 6 July 2026

reaction conditions, reducing the accessibility of active sites—an issue that can be effectively mitigated by constructing core–shell architectures with carbon encapsulation. Such structures suppress metal particle aggregation through physical confinement while promoting dispersion and long-term stability of active metal species [17]. For example, Li et al. reported an $Fe_{22}@Co_{58}$ core–shell catalyst, where interphase electron transfer between the Fe core and Co shell boosted active site activity during ammonia borane hydrolysis, yielding exceptional hydrogen evolution kinetics [18]. Hong et al. developed carbon-encapsulated Co nanoparticle catalysts that leveraged the shell's physical confinement and chemical protection to achieve high catalytic efficiency and recyclability for $NaBH_4$ hydrolysis, addressing long-standing issues of aggregation and poor reusability in monometallic catalysts [19]. Collectively, these studies demonstrate that core–shell architectures enhance catalytic performance by optimizing active-site exposure, tuning electronic interactions, and improving structural stability, thereby providing a robust framework for designing high-performance borohydride hydrolysis catalysts.

Beyond structural optimization through core–shell architectures, regulating the electronic structure of active sites is critical for further improving catalytic activity. Electronic metal–support interaction (EMSI) has emerged as a powerful strategy for stabilizing ruthenium nanoparticles and enhancing catalyst performance [20,21]. This enhancement typically stems from interfacial electron transfer between the metal and the support, a process that continues until their Fermi levels equilibrate—analogous to the Mott–Schottky effect in metal–semiconductor heterojunctions [22,23]. Understanding how EMSI influences catalytic activity, selectivity, and stability has therefore become a key focus in the design of high-performance catalyst systems. Integrating the structural benefits of core–shell architectures with EMSI-mediated electronic modulation thus represents a promising pathway for overcoming the intrinsic limitations of existing catalysts.

Against this backdrop, we designed a $Co@SiO_2@C–Ru$ core-shell catalyst incorporating a $SiO_2@C$ shell layer. The SiO_2 layer provides robust confinement to suppress Co/Ru agglomeration, while the carbon layer facilitates electron transfer and mediates EMSI among the Co core, Ru sites, and the support. This architecture combines Co–Ru dual-site synergy with EMSI-driven electronic modulation, optimizing the electron density of active sites to enhance reactant adsorption and activation. Experiments revealed that the optimized $Co@SiO_2@C–Ru$ catalyst exhibited a high H_2 release rate of 7783.2 mL min^{-1} g^{-1} and maintained good stability after five cycles. This study demonstrates an effective strategy for designing highly active core–shell catalysts for $NaBH_4$ hydrolysis and broader applications in energy catalysis.

2. Experimental section

2.1. Materials

Cobaltous nitrate hexahydrate ($Co(NO_3)_2·6H_2O$, ≥99.0%, Aladdin), 1,4-dicarboxybenzene ($C_8H_6O_4$, ≥99.0%, Aladdin), tetraethyl orthosilicate ((TEOS) $C_8H_{20}O_4Si$, ≥98.0%, Aladdin), resorcinol ($C_6H_6O_2$, ≥99.0%, Aladdin), ethylenediamine ($C_2H_8N_2$, ≥99.0%, Aladdin), sodium borohydride ($NaBH_4$, ≥98.0%, Sinopharm Group), ethanol (C_2H_6O, ≥99.7%, Xilong Scientific), N,N-Dimethylformamide (DMF, C_3H_7NO, ≥99.5%, Xilong Scientific), formaldehyde solution (HCHO, 37-40%, Xilong Scientific), sodium hydroxide (NaOH, ≥96.0%, Aladdin), Ruthenium(III) chloride hydrate ($RuCl_3·xH_2O$, ≥99.95%, Aladdin). All reagents were commercially available and could be used directly without further purification. All aqueous solutions were prepared with deionized water.

2.2. Physical characterization

The field-emission scanning electron microscopy (SEM, FEI Quanta 200 FEG) and transmission electron microscopy (TEM, JEM-2100F) were used to characterize the morphology and microstructure of samples. The specific surface and pore size distribution of catalysts were calculated by Brunauer-Emmett-Teller (BET) and the Barrett-Joyner-Halenda (BJH) methods, respectively. Electron paramagnetic resonance (EPR) spectra were measured by Bruker E500 spectrometer. The surface valence of material was analyzed by X-ray photoelectron spectroscopy (XPS, JPS-9010 Mg K α). The structural integrity of samples was analyzed by X-ray diffraction (XRD, Rigaku 13 D/Max 2500 V/PC, Japan). Metal contents were investigated by inductively coupled plasma mass spectroscopy (ICP-MS, PekinElmer corporation, FLexar-NexION300X). Ultraviolet photoelectron spectroscopy (UPS) was performed using PHI5000 Versa Probe III. The Ag layer acted as a reference to measure the kinetic energy corresponding to the E_f and then the E_f was corrected to 0 eV.

2.3. Catalyst preparation

2.3.1. Synthesis of Co-MOF

According to the literature synthesis method [24], the Co-MOF precursor was prepared as follows: First, 12 mL of an ethanol solution containing Co $(NO_3)_2·6H_2O$ was added into 48 mL of a N, N-dimethylformamide (DMF) solution of terephthalic acid (0.428 g), and then stir the resulting mixture for 1 h. Next, transfer the stirred mixture into a 100 mL Teflon-lined stainless steel autoclave, heat the autoclave to 120 °C, and maintain this temperature for 12 h. Finally, allow the autoclave to cool naturally to room temperature; a purple powdery Co-MOF precursor is thus obtained.

2.3.2. Synthesis of Co-MOF@SiO_2@RF

The as-synthesized Co-MOF solution was stirred at room temperature for 30 min and subsequently ultrasonicated for another 30 min to achieve uniform dispersion. A homogeneous TEOS solution was prepared by dissolving 0.08 mL tetraethyl orthosilicate (TEOS) in a mixed solvent consisting of 16 mL deionized water and 4 mL ethanol. This TEOS solution was then introduced into the Co-MOF dispersion, and the resultant mixture was stirred at 500 rpm for 8 h under ambient conditions to yield the Co-MOF@SiO_2 solution. For the resorcinol-formaldehyde (RF) solution preparation, 0.17 g resorcinol and 0.17 mL ethylenediamine were dissolved in a 54 mL water/26 mL ethanol mixture. The solution was stirred in a 30 °C water bath for 30 min, after which 0.26 mL formaldehyde solution was added. Stirring was continued for an additional 30 min to form the RF solution. Subsequently, the Co-MOF@SiO_2 solution was added to the RF solution, and the combined mixture was stirred continuously for 48 h. The product was collected via centrifugation, alternately washed with water and ethanol, and dried in a forced-air oven at 80 °C to obtain the Co-MOF@SiO_2@RF precursor.

2.3.3. Synthesis of Co@SiO_2@C

Co-MOF@SiO_2@RF was calcined in a tube furnace under argon atmosphere at 700 °C for 2 h (3 °C/min) to obtain Co@SiO_2@C.

2.3.4. Synthesis of Co@SiO_2@C–Ru

Forty milligrams of as-synthesized Co@SiO_2@C was ultrasonically dispersed in 20 mL deionized water containing 0.0723 mmol $RuCl_3$, followed by stirring at room temperature for 4 h. Then, 15 mL of 0.09 M $NaBH_4$ solution was added dropwise, and the mixture was reacted for another 30 min. The product was collected by centrifugation, washed with water and ethanol three times, and vacuum-dried at 60 °C for 12 h (Co@SiO_2@C–$Ru_{0.0434}$, Co@SiO_2@C–$Ru_{0.0530}$, Co@SiO_2@C–$Ru_{0.0723}$ and Co@SiO_2@C–$Ru_{0.0916}$) catalysts. As mentioned above, different supports for Co–Ru and Co@SiO_2–Ru catalysts were experimentally prepared.

3. Results and discussion

3.1. Synthesis strategy and microstructure analysis

The specific synthesis procedure for the Co@SiO_2@C–Ru catalyst is illustrated in Fig. 1a. Briefly, Co@SiO_2@C was obtained by calcining Co-MOF@SiO_2@RF at 700 °C under an argon atmosphere. Subsequently, the Ru component was introduced onto Co@SiO_2@C via a $NaBH_4$ reduction, yielding the final Co@SiO_2@C–Ru catalyst. The scanning electron microscopy (SEM) image shows that the Co-MOF possesses a well-defined hexagonal morphology (Fig. 1b). After SiO_2 and RF coating, followed by calcination and Ru loading, the derived Co@SiO_2@C–Ru catalyst displays uniformly sized spherical particles (Fig. 1c), with Ru nanoparticles well dispersed across the surface. This dispersion results from the confinement and stabilizing effects of the Co@SiO_2@C core–shell support, which also provides a favorable interface for enhancing EMSI between Ru and the support. In contrast, the Co–Ru catalyst exhibits pronounced irregular agglomeration (Fig. S1a), due to the absence of a supportive interface capable of reinforcing EMSI and suppressing particle aggregation. Co@SiO_2–Ru shows a relatively loose morphology with reduced agglomeration, indicating that SiO_2 alone partially mitigates particle clustering but cannot effectively enhance EMSI (Fig. S1b). The transmission electron microscopy (TEM) image of Co@SiO_2@C–Ru (Fig. 1d) clearly reveals a core–shell structure with uniform spherical features. The high-resolution TEM (HR-TEM) image (Fig. 1e) and corresponding fast Fourier transform (FFT) patterns identify the crystal structure of the Co@SiO_2@C–Ru material. Lattice spacings of 0.23 nm and 0.20 nm correspond to the (100) plane of Ru and the (111) plane of Co, respectively (Fig. 1f). The selected area electron diffraction (SAED) pattern in Fig. 1g confirms the same lattice planes, further validating the successful synthesis of Co@SiO_2@C–Ru. Energy-dispersive X-ray spectroscopy (EDS) mapping shows a uniform distribution of Ru, Co, and Si throughout the catalyst (Fig. 1h), and quantitative EDS analysis (Table S1) further confirms their weight percentages.

For the as-synthesized Co@SiO_2@C–Ru catalyst, its X-ray Diffraction (XRD) pattern (Fig. 2a) shows distinct peaks at 44.0° and 51.5°, corresponding to the (111) and (200) planes of metallic Co (PDF#15-0806), respectively. Meanwhile, the characteristic Raman signals of SiO_2 are hardly observed, which is attributed to the amorphous nature of silica in

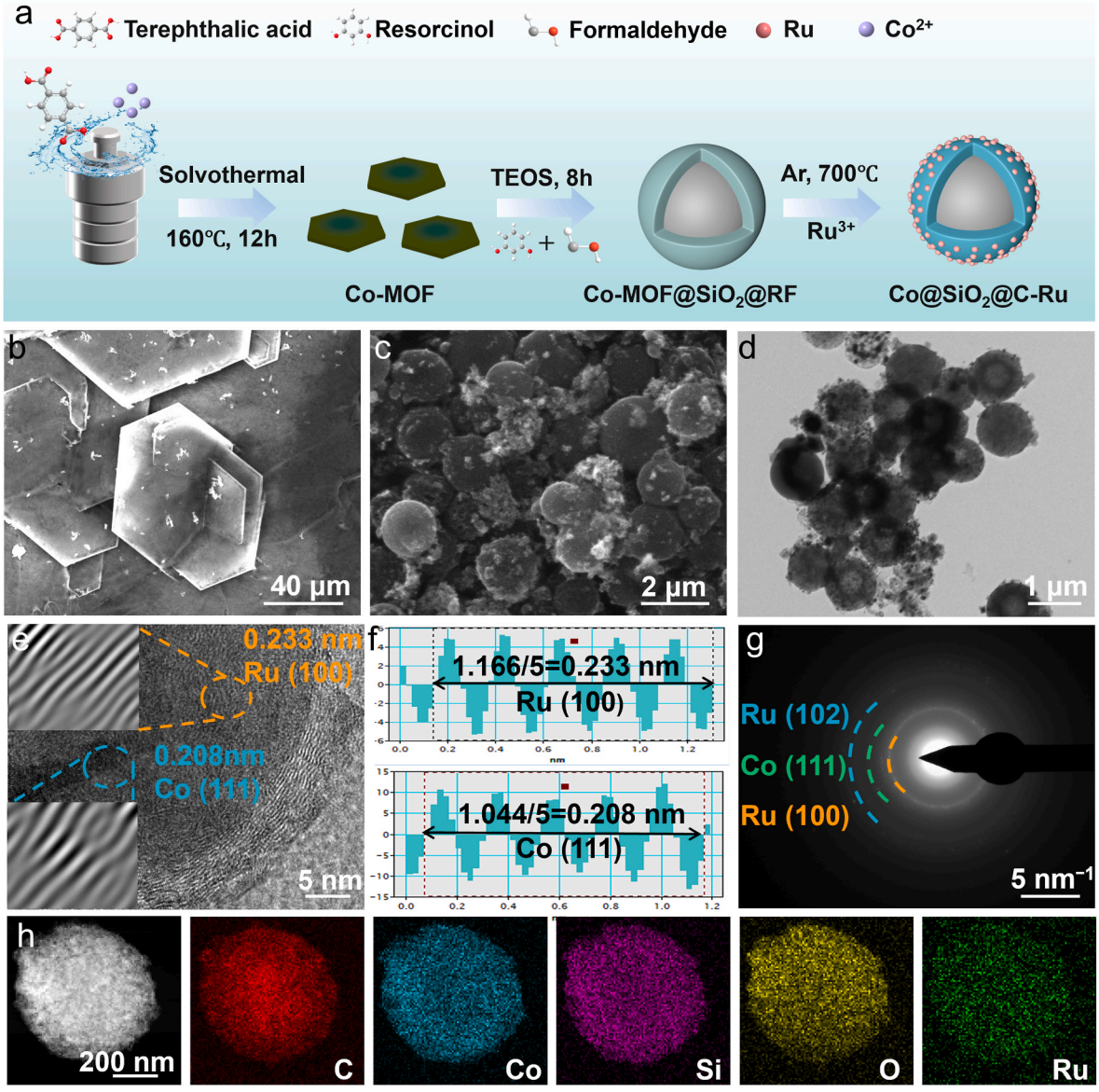

Fig. 1. (a) Scheme for the synthesis of Co@SiO_2@C–Ru. SEM images of (b) Co-MOF and (c) Co@SiO_2@C–Ru. (d) TEM image, (e) HR-TEM image, (f) the lattice spacing profiles of Ru and Co, (g) SAED pattern, and (h) HAADF-STEM images and the corresponding elemental mappings of Co@SiO_2@C–Ru.

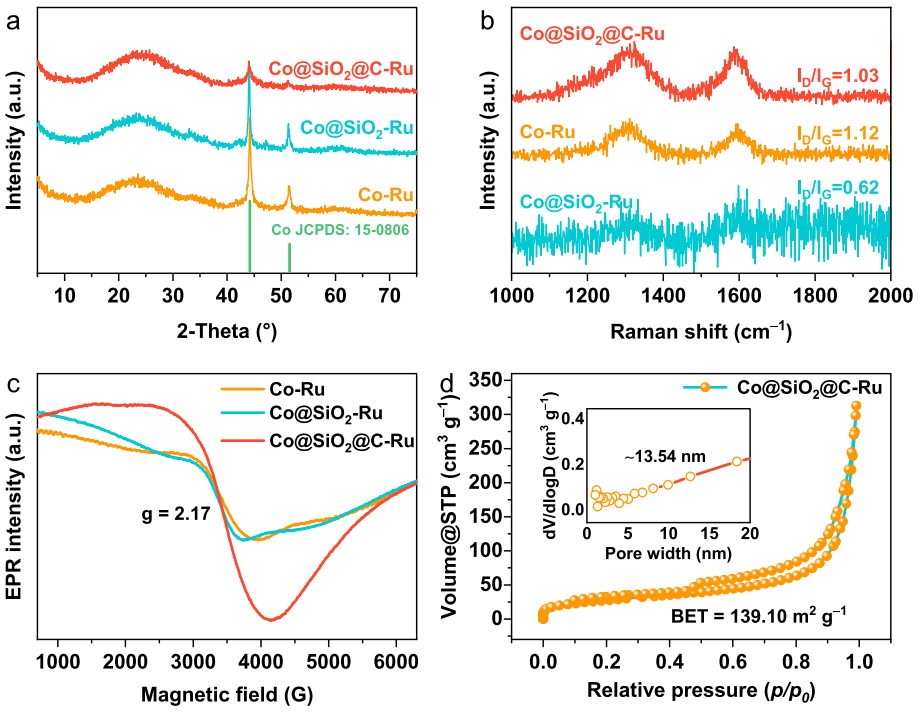

Fig. 2. (a) XRD patterns, (b) Raman spectra, and (c) EPR spectra of the different catalysts. (d) N_2 adsorption–desorption isotherm of Co@SiO_2@C–Ru (inset: corresponding pore size distribution curve).

the carbon spheres [25]. The XRD patterns in Fig. S2 further confirm the successful synthesis of Co-MOF and verify that its structural integrity is preserved after SiO_2 coating. Raman spectroscopy was employed to characterize the degree of graphitization of the carbon framework. As shown in Fig. 2b, two characteristic Raman peaks appear at ~1345 and ~1585 cm^{-1}, corresponding to the disorder-induced D band and the tangentially stretched G band of carbon, respectively [1]. The intensity ratio (I_D/I_G) is commonly used to evaluate the defect density of carbon materials. The I_D/I_G ratios of Co@SiO_2@C–Ru, Co@SiO_2–Ru, and Co–Ru were calculated to be 1.03, 0.62, and 1.12, respectively. Although Co–Ru possesses the highest defect density, its severe Ru agglomeration (Fig. S1a) prevents effective utilization of these defects. Co@SiO_2@C–Ru maintains a moderately high defect level (1.03), which facilitates electron transfer while preserving structural integrity, contributing synergistically to the catalytic performance [26,27]. Electron paramagnetic resonance (EPR) spectra reveal the presence of Co defects at g = 2.17 in Co@SiO_2@C–Ru (Fig. 2c). Compared with Co@SiO_2–Ru and Co–Ru, Co@SiO_2@C–Ru exhibits a stronger EPR signal [28]. The abundant cobalt vacancies and associated unpaired electrons significantly modulate the local electronic structure and orbital coupling, facilitating the exposure of more active sites and improving the adsorption of reactive intermediates [29]. Additionally, the N_2 adsorption–desorption isotherms of Co@SiO_2@C–Ru exhibit a type-IV isotherm with a pronounced hysteresis loop, indicating the coexistence of micropores and mesopores (Fig. 2d) [2,30]. Specifically, the BET measurements further reveal that Co@SiO_2@C–Ru, Co@SiO_2–Ru, and Co–Ru possess specific surface areas of 139.10, 138.10, and 167.42 $m^2\ g^{-1}$, with average pore sizes of 13.54, 9.24, and 10.95 nm, respectively (Fig. S3a–b). The high surface area and hierarchical porosity—particularly the enlarged pore size of Co@SiO_2@C–Ru—are expected to expose abundant active sites and promote electrolyte penetration, thereby enhancing reaction kinetics [25].

The compositions and surface chemical states of Co@SiO_2@C–Ru, Co@SiO_2–Ru, and Co–Ru samples were examined by X-ray photoelectron spectroscopy (XPS). The survey spectra (Fig. S4) clearly show characteristic peaks corresponding to C, O, Ru, and Co, confirming the presence of these elements in all samples. From the high-resolution XPS spectra of C 1s + Ru 3d (Fig. 3a), the deconvoluted peaks at 284.80, 286.0, and 288.90 eV were assigned to C–C/C═C, C–O, and C═O, respectively, serving as calibration benchmarks [31]. In the same spectral region, ruthenium-related peaks were analyzed, revealing two valence states: metallic Ru^0 and oxidized RuO_2. For the Co@SiO_2@C–Ru catalyst, the Ru^0 peak appears at 281.76 eV (Fig. 3a), representing a 0.21 eV positive shift relative to the Ru^0 peaks of Co@SiO_2–Ru and Co–Ru [32]. This positive shift in the Ru^0 binding energy is attributed to a unique compressive strain effect: when subjected to strain, Ru atoms are forced closer together, increasing d-orbital overlap and broadening the d-band. To maintain the same electron filling degree, the d-band center shifts to lower energy, decreasing the density of states at the Fermi level and making Ru metal ionization more difficult—ultimately leading to an increase in Ru XPS binding energy [33]. High-resolution Co 2p XPS spectra (Fig. 3b) further complement the surface chemical state analysis, showing characteristic peaks at 778.43, 781.46, and 786.50 eV corresponding to Co^0, Co^{2+}, and a satellite peak, respectively [34,35]. Compared with Co@SiO_2–Ru and Co–Ru, the Co^0 peak in Co@SiO_2@C–Ru exhibits a slight 0.26 eV positive shift. This shift arises from electron transfer: Co donates electrons to both Ru and the carbon layer, resulting in electron depletion in both Co and Ru—manifested as synchronous positive shifts in their binding energies [36]. Additionally, the high-resolution Si 2p XPS spectrum of Co@SiO_2@C–Ru (Fig. S5) exhibits a well-defined peak at ~103 eV, characteristic of Si^{4+} in SiO_2, confirming the presence of the silica layer in the core-shell structure. Collectively, these XPS results confirm the existence of EMSI between Ru nanocrystals and the Co@SiO_2@C support. To further investigate surface electron transfer behavior, ultraviolet photoelectron spectroscopy (UPS) was conducted (Fig. 3c). The cutoff energies (E_{cutoff}) of Co@SiO_2@C–Ru, Co@SiO_2–Ru, and Co–Ru were determined to be 17.71, 20.31, and 17.19 eV, respectively. Using the equation WF = 21.22 eV−E_{cutoff} [37], the corresponding work function (WF) values were calculated to be 3.51, 0.91, and 4.03 eV—indicating that the electron escape ability of Co@SiO_2@C–Ru lies between those of Co@SiO_2–Ru and Co–Ru [38]. This intermediate electron behavior is associated with the SiO_2@C multi-layer encapsulation: the carbon layer

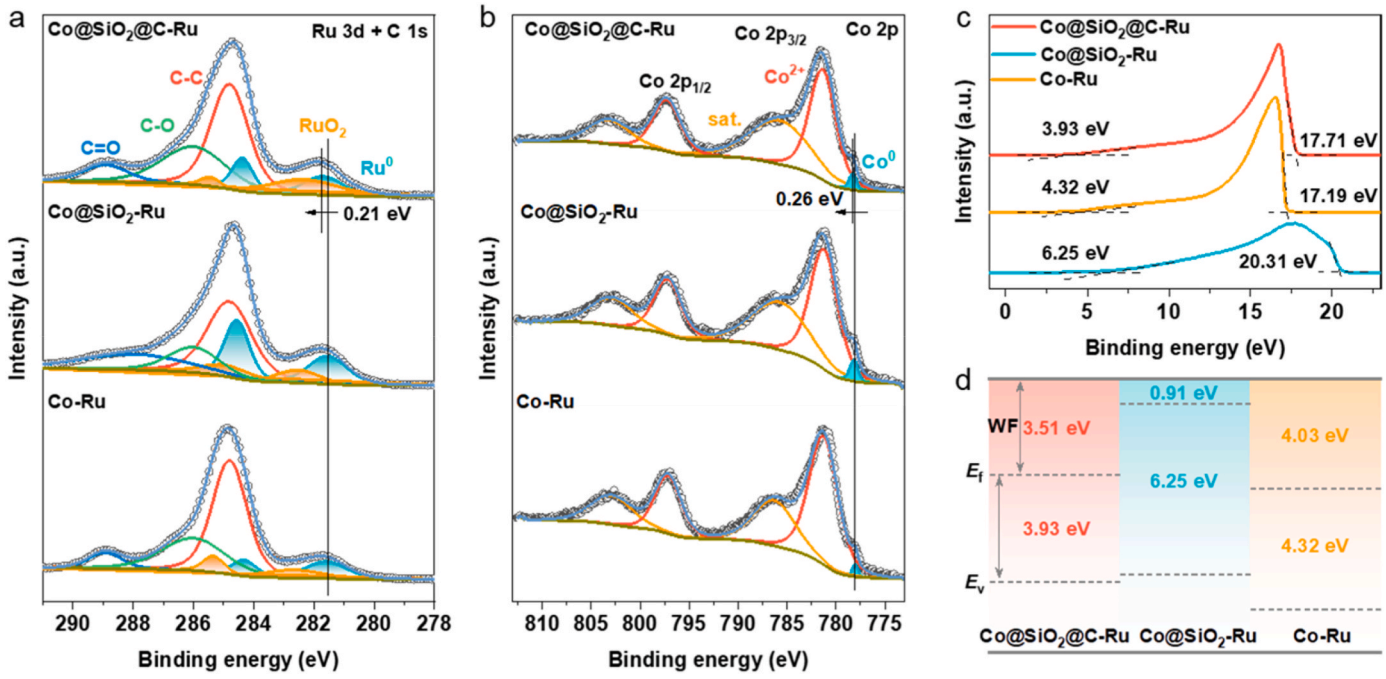

Fig. 3. High-resolution XPS spectra of (a) Ru 3d + C 1s and (b) Co 2p are shown for Co@SiO_2@C–Ru, Co@SiO_2–Ru, and Co–Ru. (c) UPS spectra and (d) corresponding energy-band alignment diagram of Co@SiO_2@C–Ru, Co@SiO_2–Ru, and Co–Ru.

promotes electron delocalization, whereas the insulating SiO_2 layer restricts electron transport, producing a balanced electron escape capability. Additionally, the valence band maximum (VBM) values of Co@SiO_2@C–Ru, Co@SiO_2–Ru, and Co–Ru were measured as 3.93 eV, 6.25 eV, and 4.32 eV, respectively (Fig. 3d). Notably, the valence band of Co@SiO_2@C–Ru lies closer to the Fermi level (E_f), which enhances the catalyst's adsorption capacity toward reactants [39].

3.2. *Catalytic hydrogen production from $NaBH_4$ hydrolysis*

The catalytic activity of the catalysts for $NaBH_4$ hydrolysis was evaluated at 25 °C. Previous studies have shown that aqueous $NaBH_4$ solutions undergo slight self-decomposition (Fig. S6a), whereas the system exhibits superior stability in alkaline media (Fig. S6b) [40]. Therefore, an alkaline $NaBH_4$ solution was selected for subsequent catalytic tests, as it effectively suppresses spontaneous decomposition and prevents interference with catalytic activity evaluation. Experimental results (Fig. 4a and b) indicate the following order of hydrogen production rates: Co@SiO_2@C–Ru > Co–Ru > Co@SiO_2–Ru > Co. Among these, the Co@SiO_2@C–Ru catalyst exhibits the highest hydrogen production rate (7783.2 mL min^{-1} g^{-1}), which is attributed to the synergistic effect between Co and Ru dual active sites—modulated by EMSI [41]. Further investigation of Ru loading (Fig. 4c–d) shows that Co@SiO_2@C–Ru catalysts with different Ru contents exhibit similar H_2 evolution behavior: a rapid initial increase followed by a plateau. This is because excessive Ru tends to aggregate into larger particles, reducing the interfacial contact area between Ru and Co@SiO_2@C, weakening EMSI, and thus limiting catalytic activity. Considering both cost and hydrogen production efficiency, 0.0725 mmol Ru was determined to be the optimal loading. The Ru content in the optimized Co@SiO_2@C–Ru catalyst, determined by ICP-MS (Table S2), was 7.9 wt%. Table S3 compares the catalytic performance of Co@SiO_2@C–Ru with other Ru-based catalysts reported for $NaBH_4$ hydrolysis. From the H_2 evolution profiles in Fig. 4e and f, the catalytic activity increases with increasing catalyst mass. Balancing catalytic efficiency and economic considerations, 10 mg was selected as the optimal catalyst dosage. Similarly, the effect of NaOH concentration was examined (Fig. 4g). The results show that varying NaOH concentration (0–0.8 wt%) does not significantly influence the hydrogen generation rate (HGR) [42]. Therefore, in this work OH^- primarily serves as a stabilizer to prevent $NaBH_4$ self-hydrolysis, while its direct kinetic regulation on Co@SiO_2@C–Ru is negligible over the tested concentration range. Fig. 4h displays the H_2 evolution curves at various $NaBH_4$ concentrations using Co@SiO_2@C–Ru. Although the total hydrogen volume increases with $NaBH_4$ concentration, the hydrogen evolution rate increases only marginally. The corresponding logarithmic plot shows a slope of 0.046, indicating that the hydrolysis reaction is close to zero-order with respect to $NaBH_4$ concentration (Fig. 4i) [43]. Combining this kinetic feature with the structural evidence from XPS and UPS, we can now clearly rank the contributions of different factors. The porous structure and carbon defects play supportive roles in mass transfer and electron transport, whereas the EMSI-modulated Co–Ru dual-site synergy is the dominant contributor to the high hydrogen generation rate.

To further investigate the catalyst's activation energy, HGR was measured over the temperature range from 298 K to 313 K. As shown in Fig. 5a and Fig. S7, the hydrogen production rates of both Co@SiO_2@C–Ru and Co–Ru (reflected by the slopes of the H_2 evolution curves) increase significantly with rising temperature. Fig. 5b shows that the activation energies for Co@SiO_2@C–Ru and Co–Ru are 57.07 and 42.78 kJ mol^{-1} respectively. Although Co@SiO_2@C–Ru has a higher activation energy than Co–Ru, its superior performance can be attributed to multiple factors, including a higher density of surface-active sites, a synergistic effect between Co and Ru dual active sites, and an optimized electronic structure via EMSI that facilitates electron transfer and reactant activation [44]. The Co@SiO_2@C–Ru catalyst retains 62% of its initial hydrogen generation rate after five consecutive cycles (Fig. 5c and d), demonstrating moderate recycling stability. To further clarify the activity decay behavior, the structural and surface electronic properties of the fresh and cycled catalysts were systematically compared. XRD characterization indicates that the phase composition of the used Co@SiO_2@C–Ru catalyst remains nearly unchanged compared with the fresh catalyst (Fig. S8), confirming its structural stability during reaction. In contrast, XPS analysis reveals a significant reduction in the intensity of Ru characteristic peaks after reaction (Fig. S9 and Fig. S10), indicating that Ru species detach from the catalyst surface. The decline

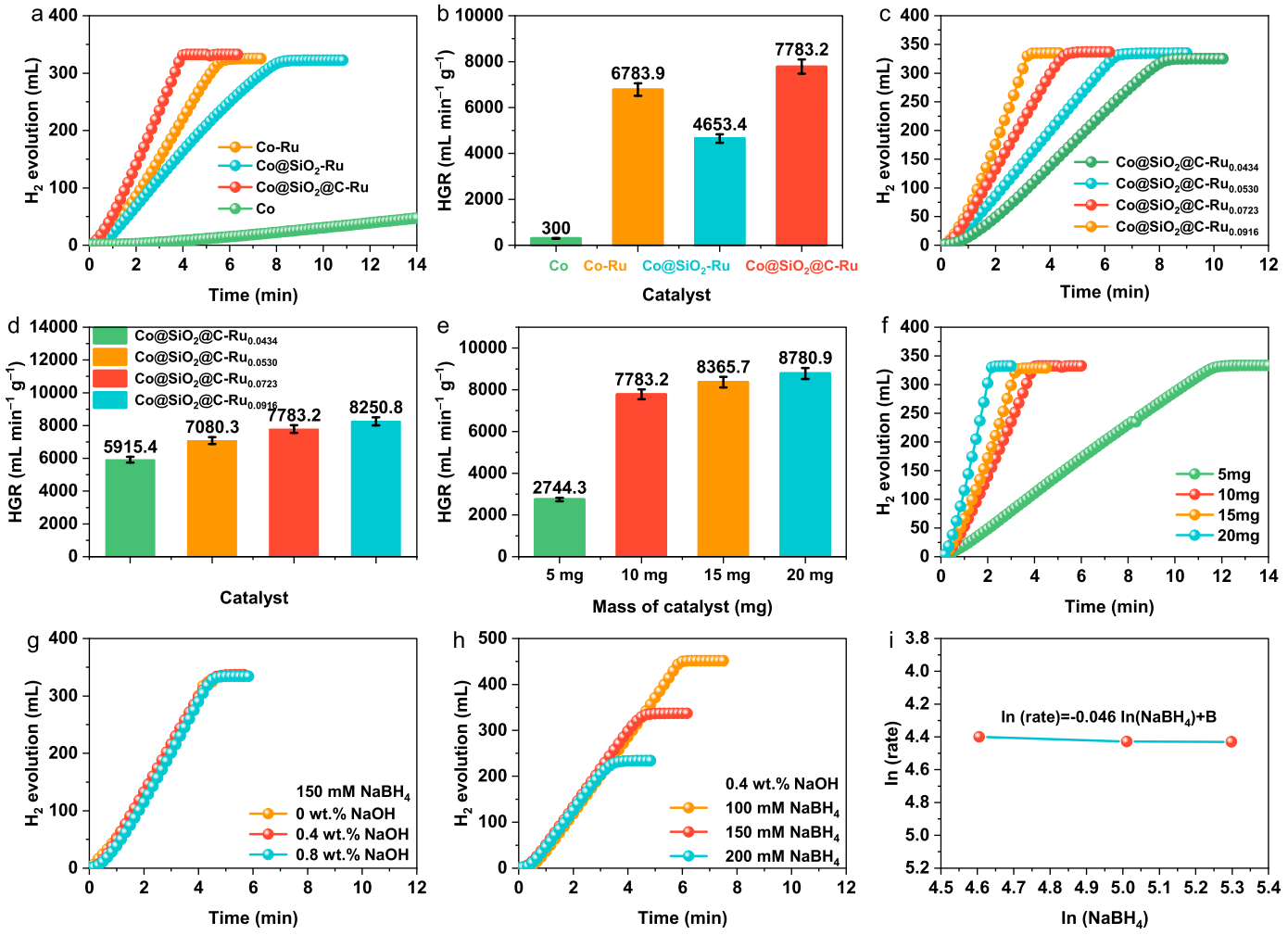

Fig. 4. (a) Time-dependent H_2 evolution curves of different catalysts. (b) Histogram of hydrogen generation rate for different catalysts. (c) Time-dependent H_2 evolution volume profiles over $Co@SiO_2@C–Ru$ catalysts with different Ru loadings (the subscripts denote the molar amount of Ru). (d) Histogram of hydrogen generation rate derived from the time-dependent profiles over $Co@SiO_2@C–Ru$ catalysts with different Ru loadings. (e) H_2 evolution over time with varying catalyst masses. (f) HGR as a function of catalyst mass. (g) H_2 evolution over time under different NaOH concentrations. (h) H_2 evolution over time under different $NaBH_4$ concentrations. (i) The plot of H_2 generation rate versus the concentration of $NaBH_4$ on a natural logarithmic scale.

in catalytic activity during recycling arises mainly from two factors: first, the accumulation of reaction by-product $NaBO_2$ that covers the metal active sites [45]; second, the detachment of Ru species from the catalyst surface.

3.3. Catalytic hydrolysis mechanism

Based on the hydrolysis results, the $Co@SiO_2@C–Ru$ catalyst exhibits superior performance, and thus the possible catalytic hydrolysis mechanism is proposed according to the Michaelis–Menten model [46–49] and illustrated in Fig. 5e Specifically, BH_4^- preferentially adsorbs on the Ru active sites—benefiting from the optimized electron density arise from EMSI, which enhances the affinity of Ru for BH_4^-. This adsorption triggers the dissociation of B–H bonds into $*H^-/*BH_3$ intermediates, accompanied by electron transfer. Meanwhile, H_2O molecules adsorb onto Co active sites and dissociate into H^+ and $*OH^-$. The $*H^-$ species on Ru sites subsequently react with H^+ generated on Co sites to release H_2, whereas $*BH_3$ combines with $*OH^-$ to form the $*BH_3OH^-$ intermediate, which then re-adsorbs onto Ru sites for further cyclic B–H bond cleavage. Ultimately, each BH_4^- molecule is converted into four H_2 molecules and $B(OH)_4^-$. Notably, the porous $Co@SiO_2@C$ shell accelerates mass transfer, while EMSI-driven electron redistribution between Ru and Co ensures efficient activation of both BH_4^- and H_2O—collectively enhancing the overall catalytic activity.

4. Conclusions

In summary, a core–shell $Co@SiO_2@C$ composite was synthesized as a support to anchor Ru nanoparticles, allowing precise modulation of the EMSI between Ru and the support. Through the synergistic effect between Co and Ru, combined with experimental verification from XPS and UPS, it was confirmed that the electronic structure of Ru was effectively tuned, leading to the formation of active sites with optimized electron density. The resulting $Co@SiO_2@C–Ru$ catalyst demonstrated outstanding catalytic performance in $NaBH_4$ hydrolysis, achieving an ultrahigh hydrogen generation rate of 7783.2 mL min^{-1} g^{-1}. Moreover, the catalyst exhibited good stability over five consecutive reaction cycles. This work presents a dual-site regulation strategy for Ru-based catalysts, offering valuable insights into the rational design of high-performance catalysts with improved metal utilization efficiency. It also contributes to the scientific foundation for efficient hydrogen storage and on-demand release systems.

Data availability

Data will be made available on request.

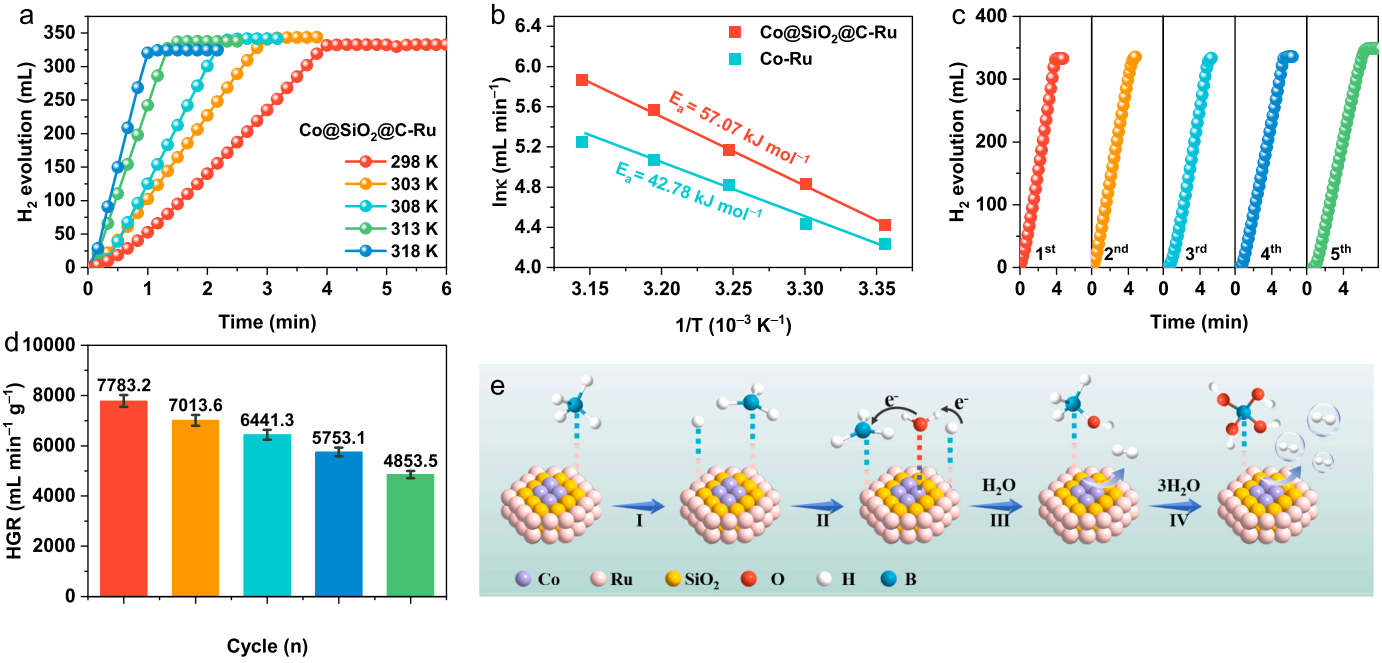

Fig. 5. (a) depicts the relationship between the H_2 generation rate and reaction temperature for Co@SiO_2@C–Ru in the hydrolysis of alkalized $NaBH_4$. (b) Arrhenius plot. (c) H_2 evolution vs. time for Co@SiO_2@C–Ru over 5 cycles. (d) HGR of Co@SiO_2@C–Ru across 5 cycles. (e) Schematic representation of the Michaelis-Menten mechanism.

CRediT authorship contribution statement

Chenxi Shang: Investigation, Writing – original draft. **Changtai Xu:** Data curation. **Boxuan Lu:** Investigation, Validation. **Shuyi Shang:** Investigation, Methodology. **Tayirjan Taylor Isimjan:** Writing – review & editing. **Jingya Guo:** Validation. **Xiulin Yang:** Supervision, Writing – review & editing.

Declaration of competing interest

The authors declare that they have no known competing financial interests or personal relationships that could have appeared to influence the work reported in this paper.

Acknowledgements

This work was financially supported by the Guangxi Science and Technology Projects (GUIKE LT2600640010), the Natural Science Foundation of Guangxi Province (2026GXNSFBA00640178), and the National Natural Science Foundation of China (52363028; W2621022; 21965005).

Appendix A. Supplementary data

Supplementary data to this article can be found online at https://doi.org/10.1016/j.ijhydene.2026.156439.

References

[1] Li Y, Huang H, Wei Q, Qiu S, Xia Y, Xu F, et al. Ruthenium nanoparticles anchored on cobalt oxide married with nitrogen and phosphorus Co-Doped carbon for hydrolytic dehydrogenation of ammonia borane. ACS Catal 2025;15:9158–70. https://doi.org/10.1021/acscatal.5c01378.

[2] Wan C, Li R, Wang J, Cheng D-g, Chen F, Xu L, et al. Silica confinement for stable and magnetic Co−Cu alloy nanoparticles in nitrogen-doped carbon for enhanced hydrogen evolution. Angew Chem Int Ed 2024;63:e202404505. https://doi.org/10.1002/anie.202404505.

[3] Wang S, Yu Y, Jiang T, Zhang T, Li Y, Sun Q. Highly dispersed cobalt phosphide in zeolites: unlocking superior efficiency in ammonia borane hydrolysis. Small 2025;21:2506106. https://doi.org/10.1002/smll.202506106.

[4] Khalil MT, Li P, Ashraf S, Mehdi S, Zhang P, Wang R, et al. Unlocking the potential of dual surface-phosphorized nickel based catalysts for enhanced hydrogen production via ammonia borane hydrolysis. J Colloid Interface Sci 2025;700:138324. https://doi.org/10.1016/j.jcis.2025.138324.

[5] Shen J, Tang M, Shi Z, Guan S, Shi Y, Zhuang Z, et al. Efficient generation of negative hydrogen with bimetallic-ternary-structured catalysts for nitrobenzene hydrogenation. Angew Chem Int Ed 2025;64:e202423626. https://doi.org/10.1002/anie.202423626.

[6] Rathod S, Gajjar D, Joshi KK, Pataniya P, Sumesh CK, Kapatel S. Catalytic hydrogen production via $NaBH_4$ hydrolysis: role of WO_3 nanopellets. Renew Energy 2025;248:123156. https://doi.org/10.1016/j.renene.2025.123156.

[7] Pham SH, Phan TS, Nguyen HN, Cong HH, Pham DK, Nguyen NL, et al. Hydrogen generation from an alkaline solution of $NaBH_4$ using a NiB catalyst supported on hydroxyapatite. J Energy Storage 2024;96:112545. https://doi.org/10.1016/j.est.2024.112545.

[8] Wang Y, Sun L, Sun Y, Xu F, Song L, Peng X, et al. Coral-like 3D-Co nanoflowers anchored on reduced graphene oxide for enhancing hydrogen generation of $NaBH_4$. J Alloys Compd 2025;1032:181241. https://doi.org/10.1016/j.jallcom.2025.181241.

[9] Ouyang L, Chen W, Liu J, Felderhoff M, Wang H, Zhu M. Enhancing the regeneration process of consumed $NaBH_4$ for hydrogen storage. Adv Energy Mater 2017;7:1700299. https://doi.org/10.1002/aenm.201700299.

[10] Ezz-Elregal E-EM, Shinohara K, El-Hosainy H, Miyakage T, Toyao T, Shimizu K-i, et al. A catalyst for sodium borohydride dehydrogenation based on a mixed-valent iron hydroxide platform. ACS Catal 2025;15:12269–80. https://doi.org/10.1021/acscatal.5c01894.

[11] Han Y, Yang X, Xu F, Wang Y, Liu W, Ma J, et al. Cobalt-manganese-boron/nickel foam for hydrogen generation from the hydrolysis of sodium borohydride solution. Renew Energy 2025;246:122899. https://doi.org/10.1016/j.renene.2025.122899.

[12] Urgnani J, Torres FJ, Palumbo M, Baricco M. Hydrogen release from solid state $NaBH_4$. Int J Hydrogen Energy 2008;33:3111–5. https://doi.org/10.1016/j.ijhydene.2008.03.031.

[13] Xie S, Tian S, Yang J, Wang N, Wan Q, Wang M, et al. Synergizing Mg single atoms and Ru nanoclusters for boosting the ammonia borane hydrolysis to produce hydrogen. Angew Chem Int Ed 2025;64:e202424316. https://doi.org/10.1002/anie.202424316.

[14] Xu W, Li W, Chen W, Liu M, Guo X, Li B. In situ formed nickel phosphide/iron oxide heterojunction for accelerating hydrogen generation. Green Chem 2024;26:5409–16. https://doi.org/10.1039/D4GC00393D.

[15] Zhang J, Quast T, Eid B, Chen Y-T, Zerdoumi R, Dieckhöfer S, et al. In-situ electrochemical reconstruction and modulation of adsorbed hydrogen coverage in cobalt/ruthenium-based catalyst boost electroreduction of nitrate to ammonia. Nat Commun 2024;15:8583. https://doi.org/10.1038/s41467-024-52780-x.

[16] Li J, Hou C, Chen C, Ma W, Li Q, Hu L, et al. Collaborative interface optimization strategy guided ultrafine RuCo and MXene heterostructure electrocatalysts for efficient overall water splitting. ACS Nano 2023;17:10947–57. https://doi.org/10.1021/acsnano.3c02956.

[17] Wei X, Zhang X, Jin L, Yang X, Zou W, Gao B, et al. Waste biomass-derived biochar in adsorption-photocatalytic conversion of CO_2 for sustainable energy and

environment: evaluation, mechanism, and life cycle assessment. Appl Catal B Environ Energy 2024;351:123957. https://doi.org/10.1016/j.apcatb.2024.123957.
[18] Huo J, Fu L, Zhao C, He C. Hydrogen generation of ammonia borane hydrolysis catalyzed by $Fe_{22}@Co_{58}$ core-shell structure. Chin Chem Lett 2021;32:2269–73. https://doi.org/10.1016/j.cclet.2020.12.059.
[19] Li J, Hong X, Wang Y, Luo Y, Huang P, Li B, et al. Encapsulated cobalt nanoparticles as a recoverable catalyst for the hydrolysis of sodium borohydride. Energy Storage Mater 2020;27:187–97. https://doi.org/10.1016/j.ensm.2020.01.011.
[20] Duan X, Niu B, Wang Y, Yang Z, Ren H, Li G, et al. Regulating the electronic metal–support Interaction of single-atom ruthenium catalysts for boosting chlorobenzene oxidation. Environ Sci Technol 2025;59:7408–18. https://doi.org/10.1021/acs.est.5c00299.
[21] Li Z, Yang Y, Zhang C, Fan W, Li G, Fang J, et al. Atomically engineering the metal-support interaction of single-atom Cu/TiO_2 for efficient polyethylene terephthalate plastic photoreforming. Chem Catal 2024;4:100902. https://doi.org/10.1016/j.checat.2024.100902.
[22] Campbell CT. Electronic perturbations. Nat Chem 2012;4:597–8. https://doi.org/10.1038/nchem.1412.
[23] Rao RG, Blume R, Greiner MT, Liu P, Hansen TW, Dreyer KS, et al. Oxygen-doped carbon supports modulate the hydrogenation activity of palladium nanoparticles through electronic metal–support interactions. ACS Catal 2022;12:7344–56. https://doi.org/10.1021/acscatal.2c01063.
[24] Zhang H, Fan Y, Liu B, Liu Y, Ashraf S, Wu X, et al. Birdcage-type CoOx-Carbon catalyst derived from metal–organic frameworks for enhanced hydrogen generation. ACS Sustainable Chem Eng 2019;7:9782–92. https://doi.org/10.1021/acssuschemeng.8b06660.
[25] Wang J, Gao C, Yang Z, Zhang M, Li Z, Zhao H. Carbon-coated mesoporous silicon shell-encapsulated silicon nano-grains for high performance lithium-ion batteries anode. Carbon 2022;192:277–84. https://doi.org/10.1016/j.carbon.2022.02.063.
[26] Dong Y, Chen G, Zuo X, Li J, Yu J, Zhang G, et al. Nitrogen, sulfur Co-doped hollow Carbon-encapsulated Cu/Co_2P for selective oxidation esterification of furfurals. ACS Catal 2024;14:6565–76. https://doi.org/10.1021/acscatal.4c01035.
[27] Wang J, Liu S, Song P, Zhang X, Song Y, Guo W, et al. Highly efficient activation of molecular oxygen by Cu@N doped carbon for antibiotic degradation. Chem Eng J 2025;507:160769. https://doi.org/10.1016/j.cej.2025.160769.
[28] Sun J, Xue H, Guo N, Song T, Hao Y-r, Sun J, et al. Synergetic metal defect and surface chemical reconstruction into $NiCo_2S_4$/ZnS heterojunction to achieve outstanding oxygen evolution performance. Angew Chem Int Ed 2021;60:19435–41. https://doi.org/10.1002/anie.202107731.
[29] Lei X, Wang J, Wang T, Wang X, Xie X, Huang H, et al. Toluene decomposition by non-thermal plasma assisted $CoO_x - \gamma\text{-}Al_2O_3$: the relative contributions of specific energy input of plasma, Co^{3+} and oxygen vacancy. J Hazard Mater 2023;456:131613. https://doi.org/10.1016/j.jhazmat.2023.131613.
[30] Ma J, Yu J, Chen G, Bai Y, Liu S, Hu Y, et al. Rational design of N-doped carbon-coated cobalt nanoparticles for highly efficient and durable photothermal CO_2 conversion. Adv Mater 2023;35:2302537. https://doi.org/10.1002/adma.202302537.
[31] Gao Y, Meng W, Lv Y, Li Y, Geng Z, Niu J, et al. In situ construction of Co-CoO heterostructures on rGO-modified nickel foam for high-performance anode catalysts in direct borohydride-hydrogen peroxide fuel cells. J Energy Chem 2025;106:532–43. https://doi.org/10.1016/j.jechem.2025.02.057.
[32] Zhou S, Liu Y, Niu C, Guo J, Isimjan TT, Tian J, et al. Modulation of the d-band center through strong metal-support interaction with Ru and Cu_3P-MoP for efficient hydrogen oxidation. Chem Eng J 2025;522:167732. https://doi.org/10.1016/j.cej.2025.167732.
[33] Fan L, Shen H, Ji D, Xing Y, Tao L, Sun Q, et al. Biaxially compressive strain in Ni/Ru core/shell nanoplates boosts Li–CO_2 batteries. Adv Mater 2022;34:2204134. https://doi.org/10.1002/adma.202204134.
[34] Chen J, Ma Y, Cheng C, Huang T, Luo R, Xu J, et al. Cobalt-doped $Ru@RuO_2$ core–shell heterostructure for efficient acidic water oxidation in low-ru-loading proton exchange membrane water electrolyzers. J Am Chem Soc 2025;147:8720–31. https://doi.org/10.1021/jacs.4c18238.
[35] Chen J, Ha Y, Wang R, Liu Y, Xu H, Shang B, et al. Inner Co synergizing outer Ru supported on carbon nanotubes for efficient pH-universal hydrogen evolution catalysis. Nano-Micro Lett 2022;14:186. https://doi.org/10.1007/s40820-022-00933-2.
[36] Zhang C, Liu Y, Chang Y, Lu Y, Zhao S, Xu D, et al. Component-controlled synthesis of necklace-like hollow NiXRuy nanoalloys as electrocatalysts for hydrogen evolution reaction. ACS Appl Mater Interfaces 2017;9:17326–36. https://doi.org/10.1021/acsami.7b01114.
[37] Wei X, Song S, Cai W, Luo X, Jiao L, Fang Q, et al. Tuning the spin state of Fe single atoms by Pd nanoclusters enables robust oxygen reduction with dissociative pathway. Chem 2023;9:181–97. https://doi.org/10.1016/j.chempr.2022.10.001.
[38] Yuan M, Bai Y, Zhang J, Zhao T, Li S, He H, et al. Work function regulation of nitrogen-doped carbon nanotubes triggered by metal nanoparticles for efficient electrocatalytic nitrogen fixation. J Mater Chem A 2020;8:26066–74. https://doi.org/10.1039/D0TA08914A.
[39] Fu B, Pan W, Huang Z, Gao M, Liu B, Muhammad S, et al. Realization of efficient $4e^-$ oxygen reduction via heterojunction-phosphorus vacancy synergy for high-performance zinc–air batteries. Adv Funct Mater 2026;36:e17612. https://doi.org/10.1002/adfm.202517612.
[40] Shang C, Lu B, Wu C, Zhou S, Shi L, Isimjan TT, et al. Inducing electronic rearrangement through Co_3B-Mo_2B_5 catalysts: efficient dual-function catalysis for $NaBH_4$ hydrolysis and 4-nitrophenol reduction. Chin Chem Lett 2025;36:111152. https://doi.org/10.1016/j.cclet.2025.111152.
[41] Ni Y, Han Z, Li W, Tan J, Chai Y, Wu G, et al. Cobalt-promoted ruthenium catalysts on acidic zeolite for hydrogen production from ammonia borane hydrolysis. Chem Eng J 2025;521:167130. https://doi.org/10.1016/j.cej.2025.167130.
[42] Fernandes R, Patel N, Miotello A. Hydrogen generation by hydrolysis of alkaline $NaBH_4$ solution with Cr-promoted Co–B amorphous catalyst. Appl Catal B Environ Energy 2009;92:68–74. https://doi.org/10.1016/j.apcatb.2009.07.019.
[43] Fu F, Wang C, Wang Q, Martinez-Villacorta AM, Escobar A, Chong H, et al. Highly selective and sharp volcano-type synergistic Ni_2Pt@ZIF-8-catalyzed hydrogen evolution from ammonia borane hydrolysis. J Am Chem Soc 2018;140:10034–42. https://doi.org/10.1021/jacs.8b06511.
[44] Xu W, Li W, Liu M, Guo X, Wen H, Li B. P-bridged Fe-X-Co coupled sites in hollow carbon spheres for efficient hydrogen generation. J Colloid Interface Sci 2024;660:792–9. https://doi.org/10.1016/j.jcis.2024.01.145.
[45] Guan S, Yuan Z, Zhao S, Zhuang Z, Zhang H, Shen R, et al. Efficient hydrogen generation from ammonia borane hydrolysis on a tandem ruthenium–platinum–titanium catalyst. Angew Chem Int Ed 2024;63:e202408193. https://doi.org/10.1002/anie.202408193.
[46] Deonikar VG, Rajkamal A, Kim H. 3D hollow microrod engineered MOF-derived Cu/Co catalysts promoted by Al nanoflakes for efficient H_2 generation through $NaBH_4$ hydrolysis: perceptions on boosted reaction channels aided by a synergistic effect. Sustain Mater Technol 2023;38:e00711. https://doi.org/10.1016/j.susmat.2023.e00711.
[47] Demirci UB, Miele P. Reaction mechanisms of the hydrolysis of sodium borohydride: a discussion focusing on cobalt-based catalysts. C R Chim 2014;17:707–16. https://doi.org/10.1016/j.crci.2014.01.012.
[48] Zhou S, Yang Q, Liu Y, Cheng L, Taylor Isimjan T, Tian J, et al. Electronic metal-support interactions for defect-induced Ru/Co-Sm_2O_3 mesosphere to achieve efficient $NaBH_4$ hydrolysis activity. J Catal 2024;433:115491. https://doi.org/10.1016/j.jcat.2024.115491.
[49] Guo Q, Wang X, Yang F, Zhou S, Wei K, Zhang Y, et al. Pt single-atomic-site loaded on borate anion-intercalated $Co(OH)_2$ nanoflakes for enhanced hydrogen generation dynamics of $NaBH_4$ hydrolysis. Chem Eng J 2025;516:164141. https://doi.org/10.1016/j.cej.2025.164141.